Science Bulletin 65 (2020) 45–54

Contents lists available at ScienceDirect

Science Bulletin

journal homepage: www.elsevier.com/locate/scib

Science Bulletin
www.scibull.com

Article

Probing the active sites of site-specific nitrogen doping in metal-free graphdiyne for electrochemical oxygen reduction reactions

Xingzhu Chen [a], Wee-Jun Ong [b,c,*], Zhouzhou Kong [a], Xiujian Zhao [a], Neng Li [a,*]

[a] State Key Laboratory of Silicate Materials for Architectures, Wuhan University of Technology, Wuhan 430070, China
[b] School of Energy and Chemical Engineering, Xiamen University Malaysia, Sepang, Selangor Darul Ehsan 43900, Malaysia
[c] College of Chemistry and Chemical Engineering, Xiamen University, Xiamen 361005, China

ARTICLE INFO

Article history:
Received 23 August 2019
Received in revised form 21 September 2019
Accepted 8 October 2019
Available online 17 October 2019

Keywords:
Graphdiyne (GDY)
Site-specific nitrogen doping
Metal-free catalysts
Oxygen reduction reaction (ORR)

ABSTRACT

The development of highly active and low-cost catalysts for electrochemical reactions is one of the most attractive topics in the renewable energy technology. Herein, the site-specific nitrogen doping of graphdiyne (GDY) including grap-N, sp-N(I) and sp-N(II) GDY is systematically investigated as metal-free oxygen reduction electrocatalysts via density functional theory (DFT). Our results indicate that the doped nitrogen atom can significantly improve the oxygen (O_2) adsorption activity of GDY through activating its neighboring carbon atoms. The free-energy landscape is employed to describe the electrochemical oxygen reduction reaction (ORR) in both O_2 dissociation and association mechanisms. It is revealed that the association mechanism can provide higher ORR onset potential than dissociation mechanism on most of the substrates. Especially, sp-N(II) GDY exhibits the highest ORR electrocatalytic activity through increasing the theoretical onset potential to 0.76 V. This work provides an atomic-level insight for the electrochemical ORR mechanism on metal-free N-doped GDY.

1. Introduction

The oxygen reduction reaction (ORR), which can reduce oxygen (O_2) to hydroxyl ion (OH^-), water (H_2O) or hydrogen peroxide (H_2O_2), plays a vital role in fuel cell devices and other green energy technologies [1]. From the working principle of the fuel cell model, the kinetic of oxygen reduction on the cathode side is naturally more sluggish than that of the anodic hydrogen oxidation reaction (HOR) due to the multi-step proton-coupled electron transfer (PCET) process in ORR [2,3]. To boost the reaction rate of the cathode in fuel cells, noble metal platinum (Pt) is used as the ORR catalysts for a long time owing to its remarkable electrocatalytic performance [4]. However, Pt electrode encounters its bottleneck in large-scale commercialization on account of its cost and resource scarcity [5–7].

Researchers have made numerous efforts by far to tackle the aforementioned problem [8–11]. Herein, we have divided these strategies into two directions. One is to reduce the amount of Pt required in the catalysts on the premise of ensuring its catalytic activity, such as designing Pt-based alloys [12–15], building core–shell structures or dispersing Pt nanoparticles/single atom on other substrates [16–19]. Another approach is to develop inexpensive and earth-abundant electrocatalysts as a substitution of Pt catalyst, including non-precious metal (NPM) catalysts [20–23], carbon-based non-noble metal composites [24–28] and metal-free catalysts [29–32]. Hereinto, metal-free carbon nanomaterials are considered as promising alternatives of noble metal catalysts owing to their high specific surface areas, low costs, excellent electrical conductivities and robust chemical stabilities at room temperature [33–36].

Nowadays, compared with the well-studied carbon skeletons formed by sp^2- and sp^3- hybridized chemical bonds (e.g., graphene, carbon nanotubes and fullerenes) [37], novel carbon allotropes with topological ordered sp- and sp^2-hybridized carbon network structure have gained increasing attention for their unique structures and tunable electronic properties [38–40]. As a first synthesized member in graphynes (GYs) family [41], graphdiyne (GDY) is constructed by inserting two ethynyl units (–C≡C–) between two neighboring aromatic rings, which can be thought of a two-dimensional (2D) plane with periodically distributed pores [42]. Similar to graphene, high π-conjunction and Dirac cone also exist in GDY, which provide it with excellent surface electrical conductivity. Moreover, compared with the sp^2-hybridized carbon of

* Corresponding authors.
E-mail addresses: weejun.ong@xmu.edu.my (W.-J. Ong), lineng@whut.edu.cn (N. Li).

https://doi.org/10.1016/j.scib.2019.10.016
2095-9273/

graphene, the high-energy sp-hybridized states endow GDY with more versatility and flexibility [43]. Taking the merits of inherent characteristics, the GDY nanostructures hold huge promises in various fields such as catalysis [44–47], solar cells [48–50], supercapacitors and batteries [51–53].

Due to the chemical inertness of defect-free carbon skeleton, pristine carbon materials including graphene and GDY are not ideal catalysts for ORR electrocatalysis. Heteroatom doping, which can induce partial charge change on the neighboring carbon, is regarded as a research frontier in boosting the ORR electrochemical efficiency of carbon materials [54,55]. Up to now, nitrogen-containing carbon-based nanostructures, such as N-doped graphene and N-containing carbon nanotube or nanofiber, have been widely demonstrated to display superb catalytic activity in fuel cells [56–59]. Additionally, in 2018, N-doped GDY was also reported to have outstanding ORR catalytic activity with rapid kinetics and remarkable half-wave potential of $E_{1/2}$ = 0.87 V under alkaline condition, which is comparable to that of commercial Pt/C catalysts ($E_{1/2}$ = 0.86 V) [60]. Furthermore, its catalytic performance in acidic solution is slightly inferior to that of Pt/C but surpass that of other metal-free materials. Zhao et al. [60] also emphasized that by comparing with other N-doping forms, doping of N atom in the diacetylenic linkage (–C≡C–C≡C–) is the most facile approach for ameliorating the ORR activity of GDY.

Even though N-doped GDY has been experimentally proven to render robust ORR electrocatalytic activity, the atomic-level mechanism on how nitrogen influences the oxygen adsorption and reduction, to the best of our knowledge, is still ambiguous. Does the N dopant play a direct role on activating O_2 in GDY? With the question in mind, we investigated the ORR performance of GDY in three N-doping forms by means of density functional theory (DFT) calculations. Our computational results demonstrated that the N atom does not promote the ORR activity of GDY via direct bond with molecular O_2, but through modulating the charge distribution of adjacent carbon atom. Furthermore, the calculated onset potential of 0.81 V for ORR over N-doped GDY is also comparable to the previously reported theoretical potential of Pt (1 1 1) catalyst (0.78 V) [61], which is consistent with the experimental reports. As a whole, this study elucidates a clear picture for unraveling the electrochemical ORR application of metal-free N-doped GDY in a well-defined atomic level, which can also be extended to describe other metal-free carbon materials systems.

2. Computational details

2.1. Computational methods

All of the calculations were performed based on the plane-wave density functional theory (DFT) using the projected augmented wave (PAW) pseudopotentials implemented in the Vienna *ab initio* simulation package (VASP) code [62,63]. The exchange–correlation functional was described using the generalized gradient approximation in the form of Perdew-Burke-Ernzerhof (GGA-PBE) [64]. The conjugate gradient algorithm was carried out to treat the ion relaxation, and the DFT-D3 method of Grimme et al. was employed to describe the van der Waals interactions [65]. Spin-polarized calculations were performed for the radical intermediates in the reaction path. For the electronic and ionic self-consistent calculations, the convergence criteria for energy and force were set to 10^{-5} eV and 0.02 eV/Å, respectively. In this configuration, the GDY was built in a 2×2 supercell with vacuum of 20 Å in the *z*-direction, then a C atom in GDY was substituted by a N atom to form N-doped GDY. A $3 \times 3 \times 1$ Monkhorst-Pack *k*-point mesh was employed for sampling the Brillouin zone [66]. To investigate the transition states and energy barriers along the O_2 dissociation pathway, the CI-NEB method in VTST tools was carried out with a force convergence criterion of 0.08 eV/Å [67]. The free energies for the electrochemical oxygen reduction reaction were calculated using the method reported by Nørskov and co-workers [61].

2.2. Thermodynamic calculations

Four PCET steps were involved in the oxygen reduction process ($O_2 + 4H^+ + 4e^- \rightarrow 2H_2O$, E^0 = 1.23 V vs. RHE). In the alkaline fuel cells, the ORR can be denoted as $O_2 + 2H_2O + 4e^- \rightarrow 4OH^-$. It is reported that the reaction free energies for the transfer of a solvated proton can be regarded as approximations of the activation energies when the proton transfer step is downhill in energy [68]. This approach may cause a slight overestimation of activity, but it is still accurate in the qualitative analysis. Thus, we investigated the electrochemical reaction pathway via the thermodynamic reaction with the neglect of the activation barriers for each PCET step. The chemical potential (μ) of the proton-electron pair ($H^+ + e^-$) is equal to that of half a hydrogen molecule by setting the standard hydrogen electrode (SHE) as the reference electrode, $\mu(H^+ + e^-) = 1/2\ \mu(H_2)$, at U = 0 V and P_{H_2} = 101.325 kPa. The Gibbs free energy change of each PCET step can be calculated as $\Delta G = \Delta E + \Delta ZPE - T\Delta S$, where ΔE denotes the total energy difference obtained from DFT computations; ΔZPE and ΔS denote the change in zero-point energies and entropy; the temperature T is set to 298.15 K. For the simulation of H_2O in the liquid phase, the entropy of H_2O is calculated at 3.5 kPa, due to it is the equilibrium pressure of H_2O ($g \rightleftharpoons l$) at 298.15 K. The zero-point energies and entropy of adsorbates were calculated from the vibrational frequencies obtained from computations, while the entropy of molecules in gas phase was experimental values from the standard thermodynamics database. The applied electrode potential (U) is involved by shifting the energy of each PCET state by $-neU$, where n is the number of unreached proton-electron pairs. We assumed the value of pH to be zero (pH 0) for all of our calculations, and for the pH different from zero, we can use G_{pH} as the correction of the concentration-dependent H^+ free energy: $G_{pH} = 0.059 \times pH$.

3. Results and discussion

3.1. Structures, properties and stabilities of GDY and N-Doped GDY

Due to the existence of both sp- and sp^2-hybridized carbons (C^{sp}, C^{sp^2}), there are as much as four types of carbon bonds in GDY. The bond lengths are 1.44 Å for the $C^{sp^2}–C^{sp^2}$ bonds in benzene rings, 1.40 Å for the $C^{sp^2}–C^{sp^2}$ bonds close to benzene rings, 1.24 Å for the $C^{sp}–C^{sp}$ triple bonds and 1.35 Å for the $C^{sp}–C^{sp}$ single bonds linked two ethynyl units, the average bond length is attributed to the π-conjunction effect in GDY. Owing to the existence of high-energy C≡C triple bonds, the calculated chemical potential of C atom in GDY (μ = −8.48 eV) is higher than that in graphene (μ = −9.25 eV). The thermodynamics stability of GDY is not as good as graphene, however, the former is proved to play a positive role in the activation of O_2 molecule. As shown in Fig. 1, there are three types of C atom in the periodic structure of GDY, including sp^2-hybridized C atoms in the benzene rings and two types of sp-hybridized C atoms in the diacetylenic linkages. Accordingly, three types of N atom forms were taken into consideration: (1) N atoms doped in the benzene rings, named grap-N; (2) N atoms doped in diacetylenic linkages, named sp-N(I) and sp-N(II), respectively, based on the distance from the benzene rings.

The charge distributions of the catalysts are the decisive factors on their O_2 adsorption and activation properties. Table 1 shows the Bader effective charges of the atoms labeled from X0 to X5 (Fig. 1).

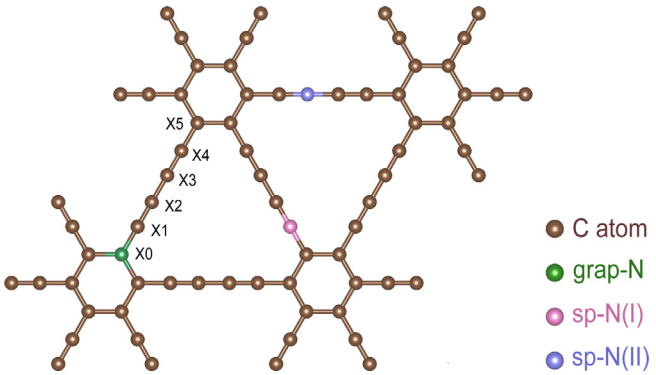

Fig. 1. (Color online) Optimized structure of graphydiyne with 2 × 2 × 1 supercell, three types of N atom forms are marked in green (grap-N), pink (sp-N(I)) and purple (sp-N(II)).

According to the Bader charge analysis, the doped N atom can induce the rearrangement of the charge distribution in the whole diacetylenic linkage. Due to the electronegativity difference between N atom and neighboring C atoms, more than 1 |*e*| is transferred from C to N atom. Thus neighboring C atoms show obvious positive charge, and the sp-N GDYs possess relatively higher degree of charge transfer compared with grap-N GDY. The doping of N atom can also decrease the band gap of GDY from 0.5 to 0.25 eV (Fig. S1 online). Furthermore, we examined the defect formation energy, $E_f = E_{\text{N-doped GDY}} - (E_{\text{GDY}} - \mu_C + \mu_N)$, to evaluate the stability of each doped system, where $E_{\text{N-doped GDY}}$, E_{GDY}, μ_C and μ_N denote the energies of N-doped GDY, GDY, one C atom in GDY as well as one N atom in nitrogen molecule (N_2), respectively. Our computation result shows that the defect formation energy of grap-N doped GDY (1.51 eV) is slightly higher than that of sp-N(I) and sp-N(II) doped GDY (0.45 and 0.78 eV), which indicates the formation of grap-N doping is more difficult than that of sp-N doping. Nevertheless, no notable geometry distortion was observed in the doped systems after 4-ps molecular dynamics simulations at 300 K (Fig. S2 online).

3.2. O_2 adsorption

The O_2 adsorption ability is the foremost prerequisite for ORR electrocatalysis, especially for metal-free materials of which adsorption activities are normally weaker than that of metals [2]. The chemical adsorption process can be written as $O_2(g) + * \rightarrow O_2*$ or $O_2(g) + 2* \rightarrow *OO*$ corresponding to O_2 end-on and side-on configuration (Fig. S3 online), where the * denotes an active site on surface.

In order to unravel the favorable adsorption sites, several initial O_2 adsorption configurations were examined on pristine GDY. We screened the adsorption sites according to the adsorption energies ($E_{ads} = E(O_2*) - (E(*) + E(O_2))$, where $E(O_2*)$, $E(*)$ and $E(O_2)$ denote the energies of the adsorbed structure, substrate and adsorbate, respectively). On account of the steric effects, high-energy distortion caused by repulsion can be observed when O_2 locates in the pores of GDY (Fig. S4 online). We then moved to discuss the O_2 adsorption properties on the carbon chains. The calculated physical O_2 adsorption energy on carbon chains ranges from –0.01 to –0.07 eV. Besides, we also observed the existence of chemical adsorption with E_{ads} of –0.32 eV in the side-on O_2 adsorption configurations. The results demonstrate that the O_2 molecules prefer to be adsorbed on the chains of GDY rather than in the pores.

After knowing the preferential adsorption sites of O_2 on GDY, we canvassed the O_2 adsorption abilities of N-doped GDY. Here, we investigated three O_2 adsorption sites on each substrate, most of the O_2 chemical adsorption configurations are side-on (Fig. 2). As demonstrated in Fig. 2a and b, the O_2 adsorption energies corresponding to Site 1 and Site 3 of pure GDY and grap-N GDY are positive. Therefore, for GDY and grap-N GDY, O_2 only can be chemically adsorbed on the ethynyl units (Site 2). This phenomenon can be attributed to the C≡C bond of the substrate underneath, which can loosen one bond to adopt the O_2 molecule. For sp-N GDY (Fig. 2c and d), the adsorption energies for three O_2 adsorption configurations are negative (from –0.36 to –1.60 eV). In addition, N doping can not only enhance the adsorption properties, but also provide more active adsorption sites. It is interesting to note the O_2 molecule does not directly bond with the sp-N atoms but dangle on the neighboring sp-hybridized C atoms, presenting an end-on adsorption configuration. According to the previous Bader charge analysis, we inferred that the sp-N atom can induce unsaturated bonds for adjacent sp-C atom to activate the C atom into active center for O_2 adsorption. In short, the O_2 chemical adsorption energies of N-doped GDY are overall lower than those of pure GDY, which demonstrates remarkable improvement of N-doped GDY in the O_2 adsorption properties.

3.3. Simple model for ORR

To assess the potential of each atom as the active sites for electrochemical ORR, we use a simple model with two PCET steps, which can be written as

$$\frac{1}{2}O_2(g) + * \rightarrow O^* \quad (1)$$

$$O^* + H_2O(l) + e^- \rightarrow OH^* + OH^- \quad (2)$$

$$OH^* + e^- \rightarrow OH^- + * \quad (3)$$

where * represents an active site on surface. In the alkaline solution, H_2O, rather than H^+, serves as the proton donor [68]. In the ideal situation, the reaction free energies of all the PCET steps should be identical, corresponding to the maximum potential of 1.23 V (equilibrium potential, $U_0 = 4.92$ eV/4*e* = 1.23 V) allowed in a fuel cell (Fig. S5 online).

Fig. 3 shows the free-energy diagram of the two-electron transfer reaction on different sites of the surface at the equilibrium potential. As shown in Fig. 3a, the value of free energy of the intermediates (O*, OH*) on C1 atom is close to zero at 1.23 V, indicating its oxygen reduction activity. However, the free energy of O* on C2 atom (0.46 eV) is higher than that of $1/2O_2$, which indicates the oxygen bonding on this atom is less stable than in the O_2 molecule.

Table 1
Bader effective charges (|*e*|) of various atoms in GDY and N-doped GDY.

GDY	X0	X1	X2	X3	X4	X5
pure	+0.12	+0.06	−0.08	−0.24	+0.06	+0.12
grap-N	−1.14[a]	+0.14	+0.34	−0.03	−0.14	+0.27
sp-N(I)	+0.44	−1.29[a]	+0.68	+0.14	−0.08	+0.26
sp-N(II)	+0.12	+0.72	−1.33[a]	+0.47	−0.05	+0.26

[a] The doping site of N atom.

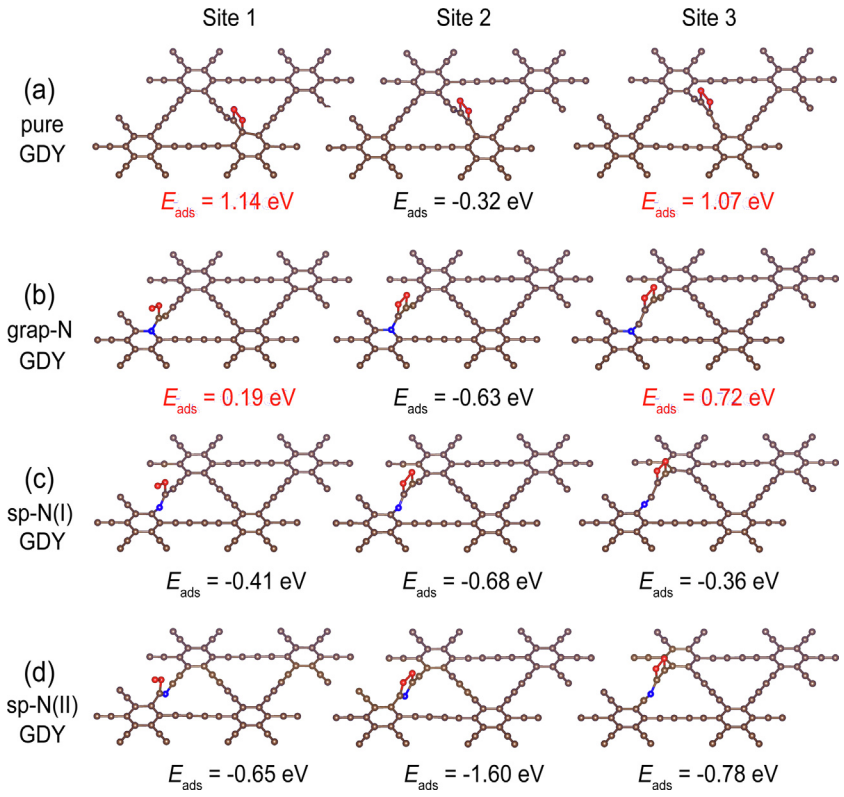

Fig. 2. (Color online) Geometric structures and the corresponding chemical adsorption energies of O_2 on GDY (a), grap-N GDY (b), sp-N(I) GDY (c) and sp-N(II) GDY(d). The brown, red and blue balls represent C, O, and N atoms, respectively.

In Fig. 3b, the free-energy values of O* are all negative, indicating that the introduce of grap-N atom will effectively enhance the O* adsorption activities of the diacetylenic chain, especially for the C atoms close to N atom. In Fig. 3c and d, similar to that on C2 atom of pure GDY, the potential of O* on sp-N atom is much higher than zero (1.10 and 1.49 eV, respectively). This matches up with the previous investigation that O_2 cannot directly bond with the N atom in N-doped GDY. In contrast, the free-energy values of O* on neighboring C atoms are greatly reduced, suggesting strong bonding between C and O atoms. In fact, the atoms that have over strong binding of O and OH, such as C1 atom with O* adsorption free energy less than −1.9 eV in sp-N-doped GDY, may also have some adversity in oxygen reduction. On the one hand, the strong binding may slow the proton-transfer steps in the hydrogenation process as well as it will prevent the desorption of OH.

Through the simple ORR model, we can make a preliminary evaluation on the oxygen reduction performance of each site. More specifically, it is an efficient way to identify the inactive sites for ORR such as C1 atom in GDY and N atom in N-doped GDY. Nevertheless, it may not denote the general trend of the overall reaction. For example, the C1 site of pure GDY shows an advantage of relatively favorable oxygen reduction properties in the simple ORR model, while it does not directly imply that GDY can serve as a good catalyst. More related details of the thermodynamics and kinetics in electrocatalytic oxygen reduction will be discussed in Section 3.4.

3.4. Electrochemical O_2 reduction mechanism

In Section 3.3, we have discussed a simple model of O_2 reduction. Herein, we will discuss the whole reaction pathways in detail starting from different O_2 adsorption sites. Apart from the adsorption sites, the O coverage rate is another important effect for the ORR performance. However, as shown in Section 3.2, the active sites of O_2 adsorption for GDY are far apart and relatively independent from each other. Thus, we only consider the situation of one adsorbed O_2 molecule around the active site. We refine the reaction pathway based on two kinds of mechanisms, including the O_2 dissociation and association mechanisms.

3.4.1. O_2 dissociation mechanism

The O_2 dissociation mechanism corresponds to the situation that O_2 dissociates into two O* after chemical adsorption on the surface (Fig. 4a). This process may occur in the O_2 molecules of which both ends bond with the surface (*OO*), so the end-on O_2 configurations with O_2 dangling on the surface (*OO) were not taken into consideration in this mechanism. The electronic oxygen reduction pathway in alkaline electrolyte is given as follow:

$$O_2(g) + 2* \rightarrow *OO* \rightarrow 2O^* \quad (4)$$

$$2O^* + H_2O(l) + e^- \rightarrow O^* + OH^* + OH^- \quad (5)$$

$$O^* + OH^* + e^- \rightarrow O^* + OH^- + * \quad (6)$$

$$O^* + H_2O(l) + e^- \rightarrow OH^* + OH^- \quad (2)$$

$$OH^* + e^- \rightarrow OH^- + * \quad (3)$$

The energy pathway of O_2 dissociation (Fig. 4b) was calculated to estimate the energy barriers on different surface (Fig. 4c). It was found that the barriers for N-doped GDY were no more than 0.2 eV, which is significantly lower than that for pure GDY (0.41 eV). Especially for sp-N GDY, the energy barrier was negligible, showing the large possibility for adsorbed O_2 to be activated into two O at the surface.

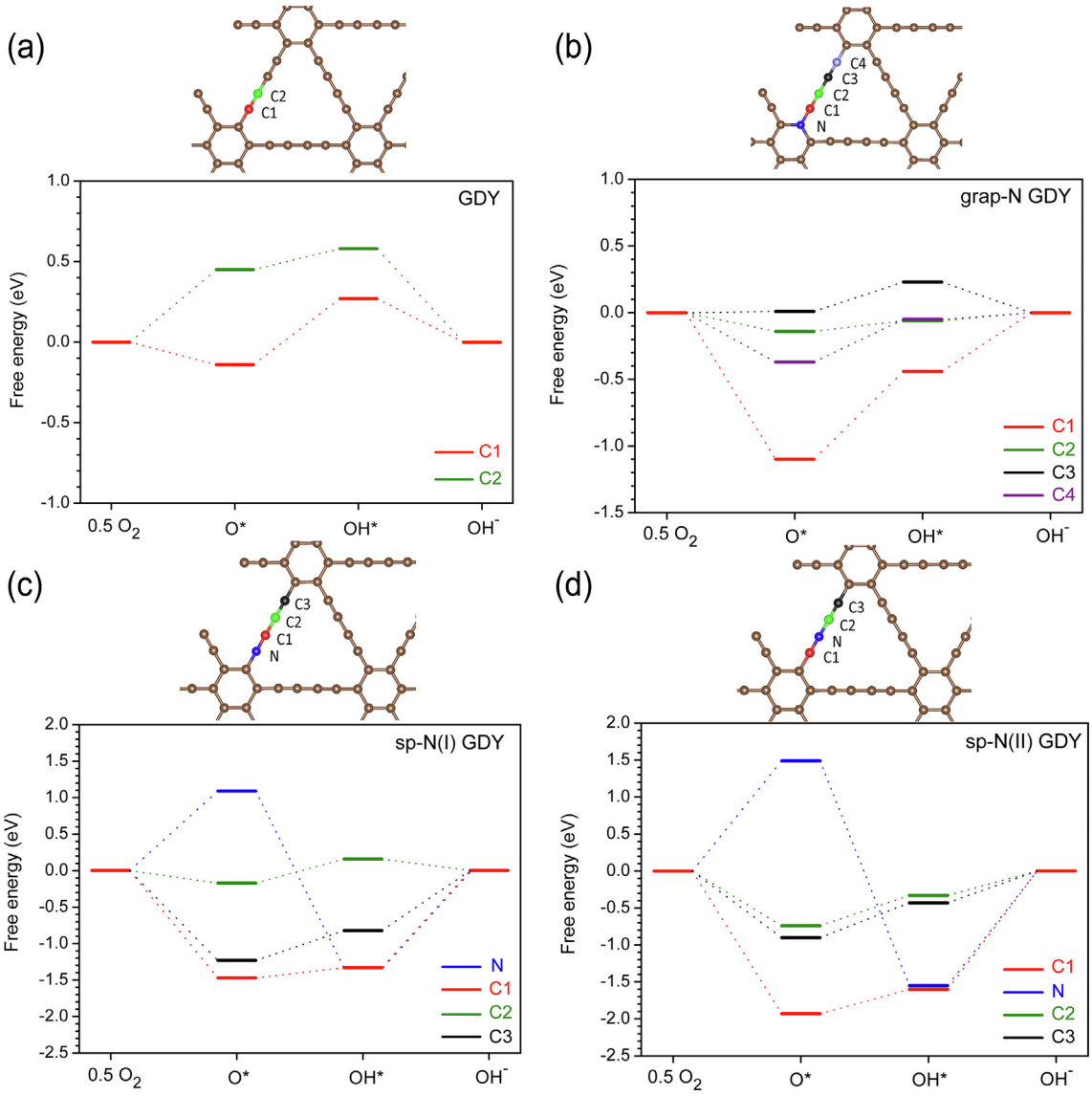

Fig. 3. (Color online) Free-energy diagram of simple ORR model ($\frac{1}{2}O_2 \rightarrow O^* \rightarrow OH^* \rightarrow OH^-$) for different sites of GDY (a), grap-N GDY (b), sp-N(I) GDY (c) and sp-N(II) GDY (d) at the equilibrium potential $U_0 = 1.23$ V.

According to the computed energy diagram for oxygen reduction over GDY, grap-N doped GDY and sp-N doped GDY (Fig. 4c–g), the thermodynamics elementary steps of oxygen reduction are spontaneously proceeding (all electron transfer steps are exothermic at zero potential). For pure GDY (Fig. 4d), when we give an onset potential of 0.12 V, the free energy of the first hydrogenation step ($2O^* \rightarrow O^* + OH^*$) will become zero, which suggests oxygen reduction cannot react spontaneously at more than 0.12 V. For grap-N GDY (Fig. 4e), sp-N(I) GDY2 (Fig. 4f), and sp-N(I) GDY3 (Fig. 4g), the thermodynamic limiting steps are the desorption of water ($OH^* \rightarrow H_2O$), and the onset potentials are 0.55, 0.51 and 0.41 V, respectively, which are higher than that of pure GDY. As shown in Fig. 4h and i, sp-N(II) GDY has some energy steps uphill in the oxygen reduction process, which manifests that O_2 cannot be spontaneously reduced to water after dissociation on sp-N(II) GDY. sp-N(II) GDY2 encounters obstacle to water desorption on account of the strong binding between C1 and O atom, which was mentioned in Section 3.3. By taking both the O_2 dissociation barriers and the ORR energy diagram into account, grap-N GDY and sp-N(I) GDY have promising performance in O_2 dissociation mechanism.

In previous theoretical study, the adsorbed state free energies of the oxygenated species (OOH*, O* or OH*) were usually used as a metric to evaluate the ORR activity [69]. However, the state of O_2 on GDY is more complicated in dissociation mechanism. To be specific, the molecular O_2 favors to locate on the top of an ethynyl unit in GDY. After dissociation, both the C atoms in the ethynyl unit will bond with one O atom, reaching an equilibrium to a certain extent. Thus, the O*+O* configuration is considerably stable ($\Delta G_{O^*+O^*} = 3.03$ eV). The small energy difference between the state of O* +O* and O* leads to the limitation in the hydrogenation step of the first O atom. By and large, for the catalysts with various orbital hybridization, it is inadequate to merely use the adsorbed state free energies of the oxygenated species to estimate their ORR activity.

3.4.2. O_2 association mechanism

Before O_2 dissociation reaction is activated on the catalytic surface, hydrogenation reaction may have taken place. As displayed in Fig. 5a, O_2 is directly reduced to a peroxy intermediate (OOH) at the surface in the first electron-transfer step instead of dissociation and then hydrogenation. To investigate the O_2 association

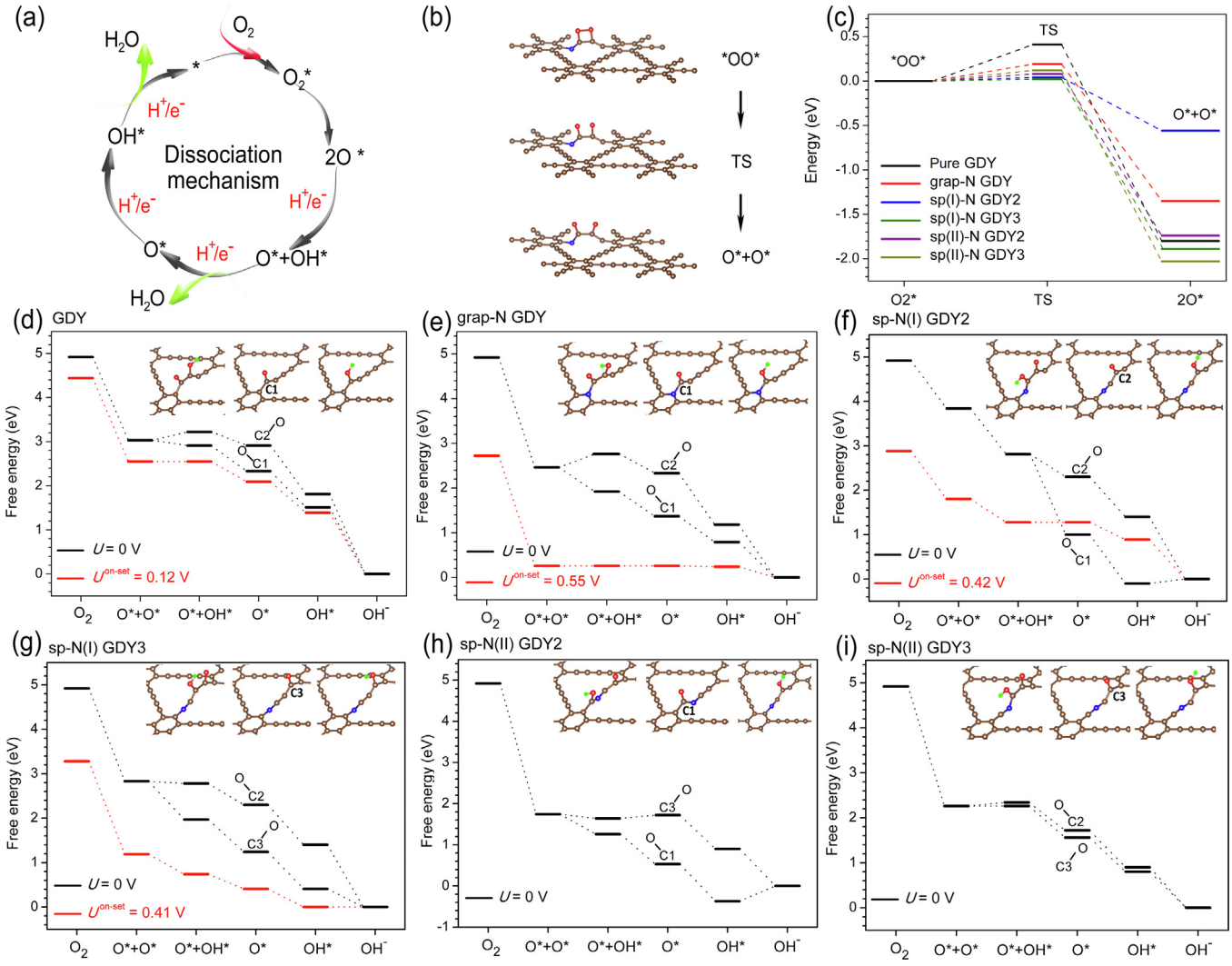

Fig. 4. (Color online) Illustration and corresponding energy diagrams of dissociation mechanism. (a) Illustration of dissociation ORR mechanism; (b) optimized geometric of O_2 dissociation on sp-N(I) GDY; (c) the energy barriers diagram of O_2 dissociation on each surface. The free-energy diagram for electrochemical ORR at zero (black line) and onset (red line) potentials over GDY (d), grap-N GDY (e), sp-N(I) GDY2 (f, g) and sp-N(II) GDY (h, i). The reaction started from different O_2 adsorption sites were labeled by GDY2 and GDY3, corresponding to O_2 adsorption site 2 and 3, respectively, as presented in Section 3.2.

mechanism, we have simulated the oxygen reduction process with reaction equations expressed as below:

$$O_2(g) + * + H_2O(l) + e^- \rightarrow OOH^* + OH^- \quad (7)$$

$$OOH^* + e^- \rightarrow O^* + OH^- \quad (8)$$

$$O^* + H_2O(l) + e^- \rightarrow OH^* + OH^- \quad (2)$$

$$OH^* + e^- \rightarrow OH^- + * \quad (3)$$

Both the end-on and side-on O_2 adsorption structures with negative chemical adsorption energies were investigated in the O_2 association mechanism. We calculated the energy diagram for the ORR association mechanism on each catalyst. As shown in Fig. 5b, the thermodynamics limiting step on pure GDY is the first hydrogenation of O_2 ($O_2 + * + H^+/e^- \rightarrow OOH^*$), which hindered the further reaction of O_2 seriously. For grap-N GDY (Fig. 5c), the potential-limiting step of the oxygen reduction process is the protonation of O* to OH*, corresponding to the onset potential of 0.58 V. From the left-most diagram in Fig. 5d and e, both the reactions, which started from dangling O_2 on sp-N GDY, have uphill steps for the desorption of OH* to water. This phenomenon has been predicted in Section 3.3 from the strong binding energy between C1 and O atom. The second and third diagrams in Fig. 5d and e demonstrate that the ORR mechanism initiated from different side-on O_2 configurations on the C2 and C3 atom of sp-N (I) GDY and sp-N(II) GDY. The onset potentials of sp-N(I) GDY2 and sp-N(I) GDY3 are 0.18 and 0.41 V, respectively. Moreover, unprecedented ORR activities of sp-N(II) GDY were obtained, recording onset potentials of 0.76 and 0.62 V, which were comparable to the theoretical prediction of Pt (1 1 1) surface (0.78 V) [61]. This is in line with the previous experimental reports [60].

For the association mechanism, we can describe the correlation of the adsorption free energies of OOH*, O* and OH* via linear functions (Fig. 6a). According to the adjusted R square (R^2) of the fitted equations, the linear relationship between ΔG(OOH*) and ΔG(OH*) is better than that between ΔG(O*) and ΔG(OH*) [70,71]. Based on the scaling relations between ΔG(OOH*), ΔG(O*) and ΔG(OH*) fitted in Fig. 6a, we depicted the limiting potential (U_i (i = 1, 2, 3, 4)) of each PCET step (as deduced in Supporting Information online). As shown in Fig. 6b, it is obvious that the value of U_2 is much more than that of others, which demonstrates that the second hydrogenation reaction ($OOH^* + H^+/e^- \rightarrow O^* + H_2O$) is a thermodynamically facile step. At the bottom of the Fig. 6b, the first

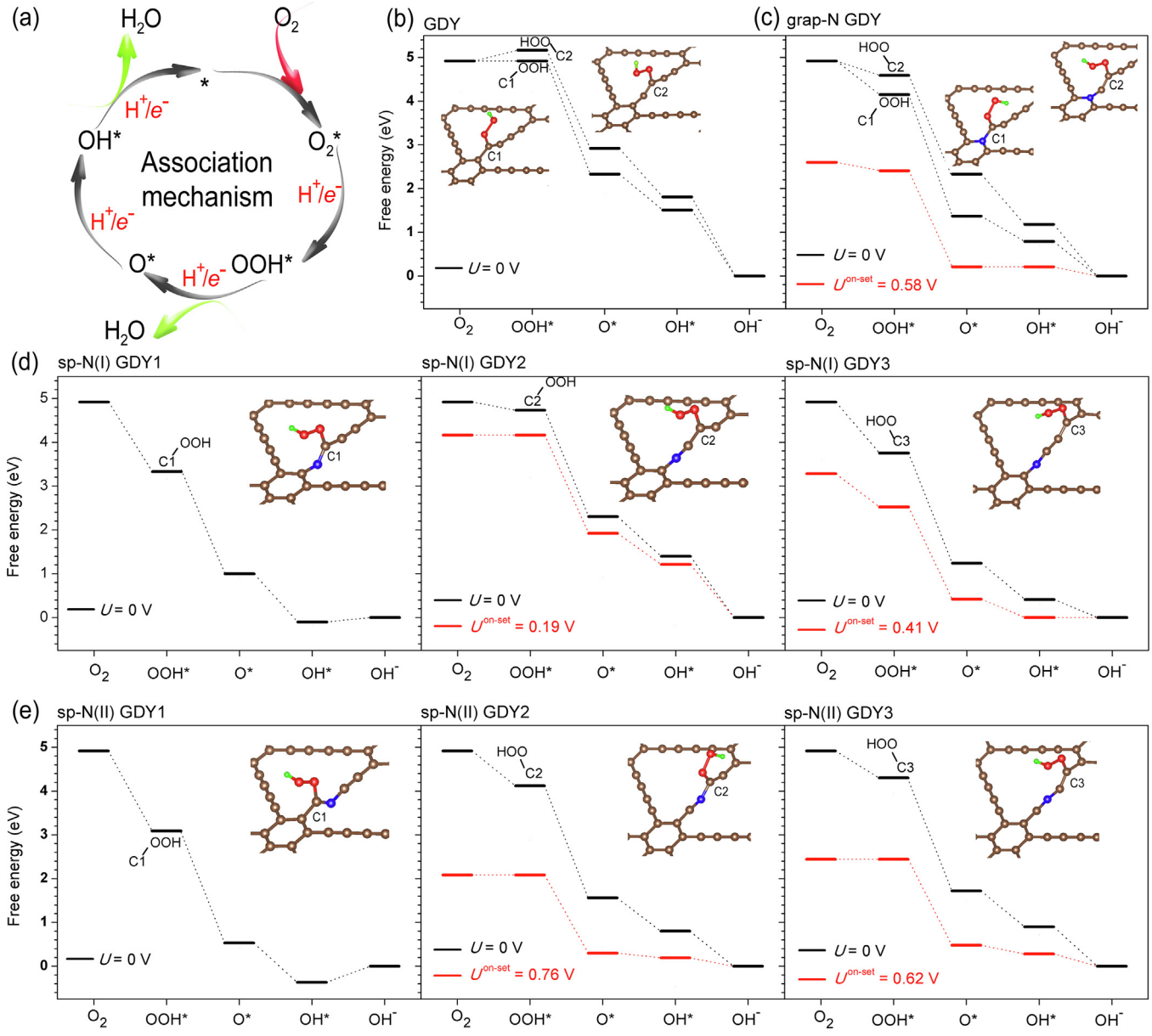

Fig. 5. (Color online) Illustration and corresponding energy diagrams of association mechanism. (a) Illustration of ORR association mechanism. The free-energy diagram for O_2 association mechanism at zero (black line) and onset (red line) potentials over GDY (b), grap-N GDY (c), sp-N(I) GDY (d) and sp-N(II) GDY (e). The reaction started from different O_2 adsorption configurations were labeled by GDY*X* (*X* = 1–3).

($O_2^* + H^+/e^- \rightarrow OOH^*$, U_1) and the forth ($OH^* + H^+/e^- \rightarrow H_2O + *$, U_4) steps determine the limiting potentials of the whole oxygen reduction reaction. U_1 goes down with the weakening of OH* adsorption (corresponding to the increase of $\Delta G(OH^*)$), while U_4 rises with that, thus U_1 and U_4 intersect with each other to form a volcano. The highest ORR thermodynamic activity with onset potential of around 0.76 V occurs at the top of volcano plot. Different from the dissociation mechanism, the adsorption free energy of OH* (optimal value ranging from 0.5 to 1.15 eV) has a direct relation with the ORR activity of N-doped GDY.

The maximum onset potentials of each catalyst for both O_2 dissociation and association mechanism are listed in Table 2 for further analysis. Compared with N-doped GDY, the pure GDY possesses a relatively higher energy barrier for O_2 dissociation and lower onset potentials of 0.12 and 0 for O_2 dissociation and association mechanism, respectively. The doping of N atom has significant contributions to the amelioration of onset electrode potential of electrocatalytic ORR on GDY. For sp-N(I) GDY, O_2 dissociation mechanism plays a dominant role for its negligible dissociation barrier (0.04 eV) and relatively higher onset potential (0.51 V) compared with that of O_2 association mechanism. Except for sp-N(I) GDY, it is evident that the ORR onset potential of association mechanism is higher than that of dissociation mechanism, especially for sp-N(II) GDY of which the onset potential can reach up to 0.76 V in O_2 association mechanism.

4. Conclusion

In summary, by means of DFT calculations, we have investigated the thermochemistry of N-doped GDY (including grap-N, sp-N(I) and sp-N(II) GDY) as effective oxygen reduction electrocatalysts. Our computation results demonstrated that O_2 molecules

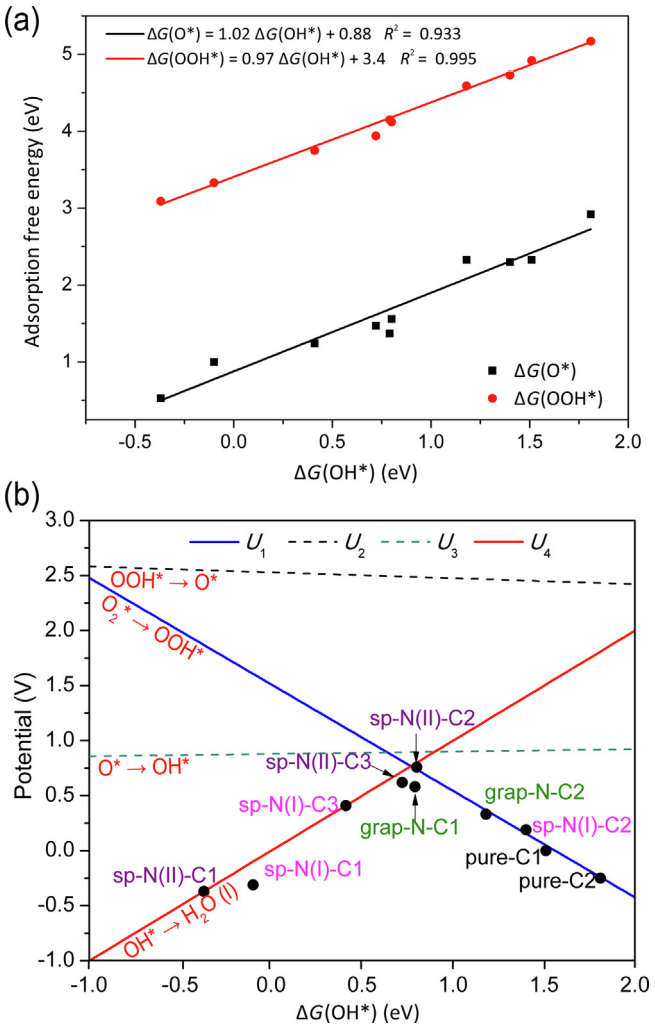

Fig. 6. (Color online) Relationship between the adsorption free energies of *OOH, *O and *OH as well as between the adsorption free energies of *OH and the ORR limiting potentials. (a) Linear relations between the adsorption free energy values of *OOH, *O and that of *OH at the active sites on GDY and N-doped GDY. (b) The volcano plot of limiting potentials for ORR activity. The ORR onset potentials for various active sites are labeled by black points.

Table 2
A comparison of dissociation barriers and onset potentials of GDY and N-doped GDY for ORR dissociation and association mechanisms.

Catalysts	Dissociation		Association
	Energy barrier (eV)	Onset potential (V)	Onset potential (V)
Pure	0.41	0.12	0
grap-N	0.19	0.55	0.58
sp-N(I)	0.04	0.51	0.41
sp-N(II)	0.12	−0.37	0.76

would rather be adsorbed on the carbon linkages than in the pores of GDY. Moreover, the doped N atom can neither bond with the molecular O_2, nor directly participate in the oxygen reduction reaction. However, doping of N atom can induce the charge redistribution, thus activating the adjacent sp-C atoms into active centers for electrocatalytic oxygen reduction. We employed the simple ORR model to screen the active sites on catalysts, followed by examining the free-energy landscape of the whole reaction in the O_2 dissociation and association mechanisms. The ORR activity for the association mechanism can be predicted by the adsorption free energy of OH* unlike for the dissociation mechanism. Our computations indicated that the onset potential of ORR in association mechanism is higher than that in dissociation mechanism, except for sp-N(I) GDY. Among the three types of N doping, sp-N(II) doping provides the most significant ORR performance improvement by increasing the onset potential to 0.76 V, which is even comparable to that of noble metal Pt (1 1 1) surface (0.78 V). As such, this work conforms to the previous experimental reports very well. To this end, we have provided a blueprint for in-depth insights into the mechanism of N-doped GDY as oxygen reduction catalysts, which can be extended to other metal-free carbon materials. At the same time, this work leaves much to be desired. For instance, the solvation effect, surface charge effect and the energetic change of electrochemical reactions caused thereby are not investigated in this work. Future work will be considered by performing the constant-potential calculations to improve the rigor of the theoretical electrochemical computations. In general, this work paves a potential avenue in demystifying the doping mechanism, which will lay a strong foundation for site-specific doping of catalysts toward a cornucopia of energy applications.

Conflict of interest

The authors declare that they have no conflict of interest.

Acknowledgments

Neng Li thanks the financial supports by the Young Scientists Fund of the National Natural Science Foundation of China (11604249), the Fok Ying-Tong Education Foundation for Young Teachers in the Higher Education Institutions of China (161008), the Foundation of the State Key Laboratory of Optical Fiber and Cable Manufacture Technology (SKLD1602), the State Key Laboratory of Refractors and Metallurgy (G201605), the Fundamental Research Funds for the Central Universities (2019-III-034), and the Research Board of the State Key Laboratory of Silicate Materials for Architectures. Wee-Jun Ong acknowledges financial supports and grants from Xiamen University Malaysia and the Xiamen University Malaysia Research Fund (XMUMRF/2019-C3/IENG/0013).

Author contributions

Wee-Jun Ong and Neng Li conceived the topic and supervised the preparation of this research article. Xingzhu Chen peroformed the theoretical calculations. Zhouzhou Kong and Wee-Jun Ong helped with the data analysis. Xingzhu Chen and Wee-Jun Ong wrote the paper. Neng Li and Xiujian Zhao revised and finalized the manuscript. All authors commented on the manuscript and approved the final version of the manuscript.

Appendix A. Supplementary materials

Supplementary materials to this article can be found online at https://doi.org/10.1016/j.scib.2019.10.016.

References

[1] Debe MK. Electrocatalyst approaches and challenges for automotive fuel cells. Nature 2012;486:43.
[2] Shao M, Chang Q, Dodelet JP, et al. Recent advances in electrocatalysts for oxygen reduction reaction. Chem Rev 2016;116:3594–657.
[3] Seh ZW, Kibsgaard J, Dickens CF, et al. Combining theory and experiment in electrocatalysis: insights into materials design. Science 2017;355:eaad4998.
[4] Macia M, Campina J, Herrero E, et al. On the kinetics of oxygen reduction on platinum stepped surfaces in acidic media. J Electroanal Chem 2004;564:141–50.
[5] Xia W, Mahmood A, Liang Z, et al. Earth-abundant nanomaterials for oxygen reduction. Angew Chem Int Ed 2016;55:2650–76.

[6] Nie Y, Li L, Wei Z. Recent advancements in Pt and Pt-free catalysts for oxygen reduction reaction. Chem Soc Rev 2015;44:2168–201.
[7] Ong WJ, Tan LL, Ng YH, et al. Graphitic carbon nitride ($g\text{-}C_3N_4$)-based photocatalysts for artificial photosynthesis and environmental remediation: are we a step closer to achieving sustainability?. Chem Rev 2016;116:7159–329.
[8] Dai L, Xue Y, Qu L, et al. Metal-free catalysts for oxygen reduction reaction. Chem Rev 2015;115:4823–92.
[9] Chen YN, Zhang X, Zhou Z. Carbon-based substrates for highly dispersed nanoparticle and even single-atom electrocatalysts. Small Methods 2019;3:1900050.
[10] Zhang L, Roling LT, Wang X, et al. Platinum-based nanocages with subnanometer-thick walls and well-defined, controllable facets. Science 2015;349:412–6.
[11] Wang X, Li Z, Qu Y, et al. Review of metal catalysts for oxygen reduction reaction: from nanoscale engineering to atomic design. Chem 2019;5:1486–511.
[12] Gocyla M, Kuehl S, Shviro M, et al. Shape stability of octahedral PtNi nanocatalysts for electrochemical oxygen reduction reaction studied by *in situ* transmission electron microscopy. ACS Nano 2018;12:5306–11.
[13] Huang X, Zhao Z, Cao L, et al. High-performance transition metal–doped Pt^3Ni octahedra for oxygen reduction reaction. Science 2015;348:1230–4.
[14] Jiang K, Zhao D, Guo S, et al. Efficient oxygen reduction catalysis by subnanometer Pt alloy nanowires. Sci Adv 2017;3. e1601705.
[15] Gan L, Rudi S, Cui C, et al. Size-controlled synthesis of sub-10 nm $PtNi_3$ alloy nanoparticles and their unusual volcano-shaped size effect on ORR electrocatalysis. Small 2016;12:3189–96.
[16] Wang Y-J, Zhao N, Fang B, et al. Carbon-supported Pt-based alloy electrocatalysts for the oxygen reduction reaction in polymer electrolyte membrane fuel cells: particle size, shape, and composition manipulation and their impact to activity. Chem Rev 2015;115:3433–67.
[17] Bu L, Zhang N, Guo S, et al. Biaxially strained PtPb/Pt core/shell nanoplate boosts oxygen reduction catalysis. Science 2016;354:1410–4.
[18] Cai B, Hübner R, Sasaki K, et al. Core-shell structuring of pure metallic aerogels towards highly efficient platinum utilization for the oxygen reduction reaction. Angew Chem Int Ed 2018;57:2963–6.
[19] Liu J, Jiao M, Lu L, et al. High performance platinum single atom electrocatalyst for oxygen reduction reaction. Nat Commun 2017;8:15938.
[20] Liang Y, Li Y, Wang H, et al. Co_3O_4 nanocrystals on graphene as a synergistic catalyst for oxygen reduction reaction. Nat Mater 2011;10:780.
[21] Sun T, Wu Q, Che R, et al. Alloyed Co-Mo nitride as high-performance electrocatalyst for oxygen reduction in acidic medium. ACS Catal 2015;5:1857–62.
[22] Tian XL, Wang L, Chi B, et al. Formation of a tubular assembly by ultrathin $Ti_{0.8}Co_{0.2}N$ nanosheets as efficient oxygen reduction electrocatalysts for hydrogen-/metal-air fuel cells. ACS Catal 2018;8:8970–5.
[23] Park H, Oh S, Lee S, et al. Cobalt- and nitrogen-codoped porous carbon catalyst made from core–shell type hybrid metal–organic framework (ZIF-L@ZIF-67) and its efficient oxygen reduction reaction (ORR) activity. Appl Catal B Environ 2019;246:322–9.
[24] Varnell JA, Edmund C, Schulz CE, et al. Identification of carbon-encapsulated iron nanoparticles as active species in non-precious metal oxygen reduction catalysts. Nat Commun 2016;7:12582.
[25] Liang H-W, Wei W, Wu ZS, et al. Mesoporous metal-nitrogen-doped carbon electrocatalysts for highly efficient oxygen reduction reaction. J Am Chem Soc 2013;135:16002–5.
[26] Wen X, Bai L, Li M, et al. Atomically dispersed cobalt- and nitrogen-codoped graphene toward bifunctional catalysis of oxygen reduction and hydrogen evolution reactions. ACS Sustainable Chem Eng 2019;7:9249–56.
[27] Li J, Chen M, Cullen DA, et al. Atomically dispersed manganese catalysts for oxygen reduction in proton-exchange membrane fuel cells. Nat Catal 2018;1:935–45.
[28] Wu ZS, Yang S, Sun Y, et al. 3D nitrogen-doped graphene aerogel-supported Fe3O4 nanoparticles as efficient electrocatalysts for the oxygen reduction reaction. J Am Chem Soc 2012;134:9082–5.
[29] Sa YJ, Kim JH, Joo SH. Active edge-site-rich carbon nanocatalysts with enhanced electron transfer for efficient electrochemical hydrogen peroxide production. Angew Chem Int Ed 2019;58:1100–5.
[30] Zhang J, Qu L, Shi G, et al. N, P-codoped carbon networks as efficient metal-free bifunctional catalysts for oxygen reduction and hydrogen evolution reactions. Angew Chem Int Ed 2016;55:2230–4.
[31] Ferrero GA, Fuertes AB, Sevilla M, et al. Efficient metal-free N-doped mesoporous carbon catalysts for ORR by a template-free approach. Carbon 2016;106:179–87.
[32] Mamtani K, Jain D, Dogu D, et al. Insights into oxygen reduction reaction (ORR) and oxygen evolution reaction (OER) active sites for nitrogen-doped carbon nanostructures (CN_x) in acidic media. Appl Catal B Environ 2018;220:88–97.
[33] Liu X, Dai L. Carbon-based metal-free catalysts. Nat Rev Mater 2016;1:16064.
[34] Yadav RM, Wu J, Kochandra R, et al. Carbon nitrogen nanotubes as efficient bifunctional electrocatalysts for oxygen reduction and evolution reactions. ACS Appl Mater Interfaces 2015;7:11991–2000.
[35] Chen X, Zhao X, Kong Z, et al. Unravelling the electrochemical mechanisms for nitrogen fixation on single transition metal atoms embedded in defective graphitic carbon nitride. J Mater Chem A 2018;6:21941–8.
[36] Jia Y, Zhang L, Zhuang L, et al. Identification of active sites for acidic oxygen reduction on carbon catalysts with and without nitrogen doping. Nat Catal 2019;2:688–95.
[37] Xu Q, Li W, Ding L, et al. Function-driven engineering of 1D carbon nanotubes and 0D carbon dots: mechanism, properties and applications. Nanoscale 2019;11:1475–504.
[38] Huang C, Li Y, Wang N, et al. Progress in research into 2D graphdiyne-based materials. Chem Rev 2018;118:7744–803.
[39] Nulakani NVR, Subramanian V. A theoretical study on the design, structure, and electronic properties of novel forms of graphynes. J Phys Chem C 2016;120:15153–61.
[40] Zhao Y, Yang N, Yao H, et al. Stereodefined codoping of sp-N and S atoms in few-layer graphdiyne for oxygen evolution reaction. J Am Chem Soc 2019;141:7240–4.
[41] Li G, Li Y, Liu H, et al. Architecture of graphdiyne nanoscale films. Chem Commun 2010;46:3256–8.
[42] Li J, Gao X, Jiang X, et al. Graphdiyne: a promising catalyst-support to stabilize cobalt nanoparticles for oxygen evolution. ACS Catal 2017;7:5209–13.
[43] Gao X, Liu H, Wang D, et al. Graphdiyne: synthesis, properties, and applications. Chem Soc Rev 2019;48:908–36.
[44] Gao Y, Cai Z, Wu X, et al. Graphdiyne-supported single-atom-sized Fe catalysts for the oxygen reduction reaction: DFT predictions and experimental validations. ACS Catal 2018;8:10364–74.
[45] Kuang P, Zhu B, Li Y, et al. Graphdiyne: a superior carbon additive to boost the activity of water oxidation catalysts. Nanoscale Horiz 2018;3:317–26.
[46] Li J, Gao X, Liu B, et al. Graphdiyne: a metal-free material as hole transfer layer to fabricate quantum dot-sensitized photocathodes for hydrogen production. J Am Chem Soc 2016;138:3954–7.
[47] Xu Q, Zhu B, Cheng B, et al. Photocatalytic H_2 evolution on graphdiyne/$g\text{-}C_3N_4$ hybrid nanocomposites. Appl Catal B Environ 2019;255:117770
[48] Kuang C, Tang G, Jiu T, et al. Highly efficient electron transport obtained by doping PCBM with graphdiyne in planar-heterojunction perovskite solar cells. Nano Lett 2015;15:2756–62.
[49] Li J, Jiu T, Duan C, et al. Improved electron transport in $MAPbI_3$ perovskite solar cells based on dual doping graphdiyne. Nano Energy 2018;46:331–7.
[50] Li J, Jiu T, Chen S, et al. Graphdiyne as a host active material for perovskite solar cell application. Nano Lett 2018;18:6941–7.
[51] He J, Wang N, Cui Z, et al. Hydrogen substituted graphdiyne as carbon-rich flexible electrode for lithium and sodium ion batteries. Nat Commun 2017;8:1172.
[52] Zhang S, Du H, He J, et al. Nitrogen-doped graphdiyne applied for lithium-ion storage. ACS Appl Mater Interfaces 2016;8:8467–73.
[53] Shen X, Yang Z, Wang K, et al. Nitrogen-doped graphdiyne as high-capacity electrode materials for both lithium-ion and sodium-ion capacitors. ChemElectroChem 2018;5:1435–43.
[54] Zhang J, Feng X. Graphdiyne electrocatalyst. Joule 2018;2:1396–8.
[55] Mamtani K, Ozkan US. Heteroatom-doped carbon nanostructures as oxygen reduction reaction catalysts in acidic media: an overview. Catal Lett 2015;145:436–50.
[56] Gong K, Du F, Xia Z, et al. Nitrogen-doped carbon nanotube arrays with high electrocatalytic activity for oxygen reduction. Science 2009;323:760.
[57] Maldonado S, Stevenson KJ. Influence of nitrogen doping on oxygen reduction electrocatalysis at carbon nanofiber electrodes. J Phys Chem B 2005;109:4707–16.
[58] Tan H, Tang J, Kim J, et al. Rational design and construction of nanoporous iron- and nitrogen-doped carbon electrocatalysts for oxygen reduction reaction. J Mater Chem A 2019;7:1380–93.
[59] Hu E, Yu X-Y, Chen F, et al. Graphene layers-wrapped Fe/Fe_5C_2 nanoparticles supported on N-doped graphene nanosheets for highly efficient oxygen reduction. Adv Energy Mater 2018;8:1702476.
[60] Zhao Y, Wan J, Yao H, et al. Few-layer graphdiyne doped with sp-hybridized nitrogen atoms at acetylenic sites for oxygen reduction electrocatalysis. Nat Chem 2018;10:924–31.
[61] Nørskov JK, Rossmeisl J, Logadottir A, et al. Origin of the overpotential for oxygen reduction at a fuel-cell cathode. J Phys Chem B 2004;108:17886–92.
[62] Kresse G, Furthmüller J. Efficiency of *ab-initio* total energy calculations for metals and semiconductors using a plane-wave basis set. Comp Mater Sci 1996;6:15–50.
[63] Kresse G, Joubert D. From ultrasoft pseudopotentials to the projector augmented-wave method. Phys Rev B 1999;59:1758.
[64] Perdew JP, Chevary JA, Vosko SH, et al. Atoms, molecules, solids, and surfaces: applications of the generalized gradient approximation for exchange and correlation. Phys Rev B 1992;46:6671–87.
[65] Grimme S, Antony J, Ehrlich S, et al. A consistent and accurate ab initio parametrization of density functional dispersion correction (DFT-D) for the 94 elements H-Pu. J Chem Phys 2010;132. 154104.
[66] Monkhorst HJ, Pack JD. Special points for Brillouin-zone integrations. Phys Rev B 1976;13:5188–92.
[67] Henkelman G, Uberuaga BP, Jónsson H. A climbing image nudged elastic band method for finding saddle points and minimum energy paths. J Chem Phys 2000;113:9901–4.
[68] Xu H, Cheng D, Cao D, et al. A universal principle for a rational design of single-atom electrocatalysts. Nat Catal 2018;1:339–48.
[69] Kulkarni A, Siahrostami S, Patel A, et al. Understanding catalytic activity trends in the oxygen reduction reaction. Chem Rev 2018;118:2302–12.

[70] Gu J, Magagula S, Zhao J, et al. Boosting ORR/OER activity of graphdiyne by simple heteroatom doping. Small Methods 2019;3:1800550.
[71] Liang W, Chen J, Liu Y, et al. Density-functional-theory calculation analysis of active sites for four-electron reduction of O_2 on Fe/N-doped graphene. ACS Catal 2014;4:4170–7.

Xingzhu Chen received her B.Eng. degree in Materials Science and Engineering from Wuhan University of Technology in 2016. She is presently working on her Ph.D. project at Wuhan University of Technology. Her research interests include photocatalysis, electrocatalysis, photoelectrochemistry, and the development of photo- and electro-catalysts for gas conversion such as N_2 fixation, O_2 reduction and CO_2 reduction using two-dimensional carbonaceous-based materials.

Wee-Jun Ong received his B.Eng. and Ph.D. degrees in Chemical Engineering from Monash University. In 2015, he was a Visiting Research Fellow in University of New South Wales and Monash University, Australia. In 2016, he joined Institute of Materials Research and Engineering (IMRE), Agency for Science, Technology and Research (A*STAR) in Singapore as a Staff Scientist. He was an Assistant Professor in the School of Energy and Chemical Engineering at Xiamen University Malaysia in 2018 and he was promoted to Associate Professor in 2019. In 2019, he is a Visiting Scientist in the Center for Advancing Electronics Dresden (CFACD) at Technische Universität Dresden, Germany. He is a Visiting Professor at the Lawrence Berkeley National Laboratory (LBNL), USA from 2019 to 2020. His research interests primarily focus on photocatalytic, photoelectrochemical and electrochemical H_2O splitting, CO_2 reduction and N_2 fixation using nanomaterials.

Neng Li received his Ph.D. degree in Condensed Matter Physics from Huazhong University of Science and Technology in 2011. Then, he joined Shenzhen Institutes of Advanced Technology, Chinese Academy of Sciences as a Research Fellow in 2011. He worked at the Department of Physics and Astronomy, University of Missouri-Kansas City as a postdoctoral researcher in 2012−2014. In 2015, he joined Wuhan University of Technology as a Full Professor. He was a Visiting Professor at the Department of Materials Science & Metallurgy, University of Cambridge, UK during 2016-2017. His research interests focus on energy and environmental applications such as photocatalysis, photocatalytic hydrogen production, CO_2 reduction, N_2 fixation, and the development of hybrid functional materials and related devices using *ab initio* calculations and molecular dynamics approach.